ACS APPLIED MATERIALS & INTERFACES

www.acsami.org

Research Article

Surface-Ligand "Liquid" to "Crystalline" Phase Transition Modulates the Solar H_2 Production Quantum Efficiency of CdS Nanorod/Mediator/Hydrogenase Assemblies

Wenxing Yang,* Gregory E. Vansuch, Yawei Liu, Tao Jin, Qiliang Liu, Aimin Ge, Monica L. K. Sanchez, Dominik K. Haja, Michael W. W. Adams, R. Brian Dyer,* and Tianquan Lian*

Cite This: https://dx.doi.org/10.1021/acsami.0c07820

Read Online

ACCESS | Metrics & More | Article Recommendations | Supporting Information

ABSTRACT: This study reports how the length of capping ligands on a nanocrystal surface affects its interfacial electron transfer (ET) with surrounding molecular electron acceptors, and consequently, impact the H_2 production of a biotic–abiotic hybrid artificial photosynthetic system. Specifically, we study how the H_2 production efficiency of a hybrid system, combining CdS nanorods (NRs), [NiFe] hydrogenase, and redox mediators (propyl-bridged 2,2′-bipyridinium, PDQ^{2+}), depends on the alkyl chain length of mercaptocarboxylate ligands on the NR surface. We observe a minor decrease of the quantum yield for H_2 production from 54 ± 6 to 43 ± 2% when varying the number of methylene units in the ligands from 2 to 7. In contrast, an abrupt decrease of the yield was observed from 43 ± 2 to 4 ± 1% when further increasing n from 7 to 11. ET studies reveal that the intrinsic ET rates from the NRs to the electron acceptor PDQ^{2+} are all within 10^8–10^9 s^{-1} regardless of the length of the capping ligands. However, the number of adsorbed PDQ^{2+} molecules on NR surfaces decreases dramatically when $n \geq 10$, with the saturating number changing from 45 ± 5 to 0.3 ± 0.1 for n = 2 and 11, respectively. These results are not consistent with the commonly perceived exponential dependence of ET rates on the ligand length. Instead, they can be explained by the change of the accessibility of NR surfaces to electron acceptors from a disordered "liquid" phase at $n < 7$ to a more ordered "crystalline" phases at $n > \sim 7$. These results highlight that the order of capping ligands is an important design parameter for further constructing nanocrystal/molecular assemblies in broad nanocrystal-based applications.

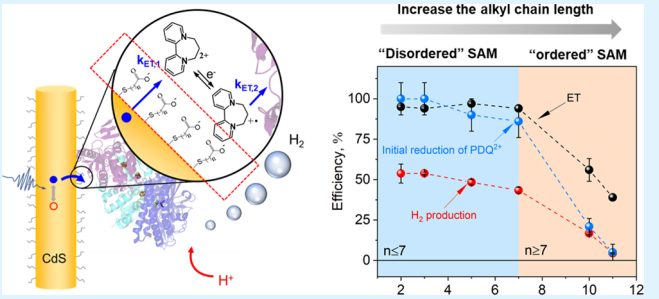

KEYWORDS: *mercaptocarboxylate, ligand configuration, self-assembly, nanocrystal, electron transfer, abiotic–biotic interface*

INTRODUCTION

The ubiquitous presence of capping ligands on the nanocrystal surface affects its interfacial electron transfer (ET) behavior and self-assembly with other materials, resulting in profound impacts on nanocrystal-based applications including triplet sensitization,[1,2] photon up-conversion,[3,4] and photocatalysis.[5,6] The chemical nature of these ligands can influence the intrinsic carrier dynamics of nanocrystals,[7] shift the nanocrystal surface energetic levels,[8−10] and form physical barriers or engineering platforms between nanocrystals with electron acceptors[11,12] or other materials.[13,14]

Recently, hybrid abiotic–biotic photosynthetic systems[15−19] based on nanocrystals and biotic enzymes have emerged as a promising approach for solar-fuel generation because they combine the superior light absorption and charge separation properties of nanocrystals[20] and the efficient, highly-selective catalytic properties of biological components. However, despite significant progress being achieved in the performance of these hybrid systems, the role of the capping ligands on these abiotic–biotic photosynthetic systems remains relatively less studied.[12] Two types of abiotic–biotic interfaces have been reported so far regarding the assemblies of nanocrystal/enzyme systems.[16−19] In the first, the direct contact approach, the nanocrystal and the charge accepting domain of the enzyme are brought into contact to allow ET directly from the nanocrystal to the enzyme active site.[12,21] In the second, the mediator approach, redox mediators shuttle electrons between the nanocrystal and enzyme that are either tethered together or freely dispersed in solution.[16,22] The latter configuration is similar to quinone-mediated ET in the natural photosystem II.[23,24] Dukovic and coworkers[12] demonstrated that the ET rate between CdS nanorod (NR) and a FeFe hydrogenase decreases exponentially with increasing the capping ligand

Received: April 28, 2020
Accepted: June 30, 2020
Published: July 14, 2020

Scheme 1. (A) Schematic Representation of the Mediator-Based CdS NR/PDQ^{2+}/[NiFe]-H_2ase Hybrid System for H_2 Production Used in the Present Study, Showing Mercaptocarboxylate Ligand-Covered CdS NRs, [NiFe]-H_2ase Tethered to the NR (through a 9×-Histidine Tag), and PDQ^{2+}-Mediated ET between the NR and H_2ase; (B) Diagram of Relevant Energy Levels (Black Lines), Optical Excitation (Gray Arrow), Forward Charge Transfer (Blue Arrows), and Backward Charge Recombination (Red Arrows) Processes of the Hybrid System

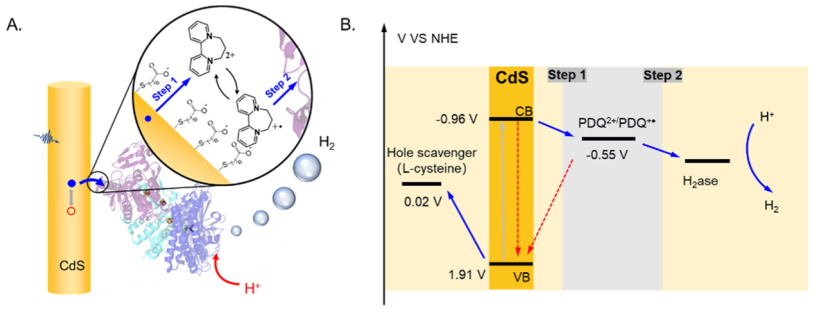

length in a direct contact approach, revealing that the ligand layer can form an ET tunneling barrier between the nanocrystal and the hydrogenase. This raises the question about how the ligand length would affect the H_2 production and ET transfer in the mediator-based nanocrystal/enzyme system, where the smaller size of the mediating electron acceptor may penetrate into the ligand layer and thus possess different length dependences.[25,26] An answer to this question can provide a rational guide toward the future design of such nanocrystal- or inorganic electrode[27,28] based-hybrid systems for artificial photosynthesis but remains unexplored.

Herein, we investigate the impact of the capping ligand length on the efficiency and ET behavior of a mediator-based hybrid photocatalytic system for H_2 generation. The system (Scheme 1) consists of CdS NRs as the light absorber, the soluble [NiFe]-hydrogenase ([NiFe]-H_2ase) from the hyperthermophilic archaeon *Pyrococcus furiosus* (*Pf*-SHI) as the enzymatic center for H^+ reduction, and propyl-bridged 2,2′-bipyridinium (PDQ^{2+}) as the redox mediator to shuttle electrons between the CdS NR and [NiFe]-H_2ase.[16] The [NiFe]-H_2ase is attached to the NR surface through a polyhistidine tag,[29] and no direct ET is measurable between CdS NRs and [NiFe]-H_2ase (see below). The operation mechanism of the system (Scheme 1A) involves first the photoreduction of PDQ^{2+} by the CdS NRs, followed by the diffusion of the reduced $PDQ^{+\bullet}$ to [NiFe]-H_2ase and transfer of its electron to a [FeS] cluster on the [NiFe]-H_2ase, which eventually transports the electron to the [NiFe] active site within the [NiFe]-H_2ase and drives the catalytic H_2 production.[16] We compare mercaptocarboxylate ligands (the most common capping ligands for water-soluble nanocrystals) with n = 2−11 $-CH_2-$ units between the thiolate and carboxylate moieties, covering the ranges of ligand length that are typically applied on the nanocrystal surface.[11,12,30] Detailed measurements of steady-state H_2 production and mediator photoreduction suggested that there exist distinct regions of ligand length-dependent quantum yields. Further ET studies characterized that the amount of surface adsorbed molecules changes dramatically when the ligand length n is above ∼7. In contrast, the intrinsic ET rate constants remain similar across all the studied ligand length range. These results indicate the existence of phase transition of capping ligands on the CdS NR surface as a function of the alkyl chain length—from disordered "liquid" and ordered "crystalline" phases—similar to that reported for thiolate ligands on Au. Further sum-frequency generation (SFG) and temperature-dependent infrared absorption spectroscopic measurements provide support for the phase transition of capping ligands. Because of the broad existence of similar nanocrystal/molecular assemblies in nanocrystal-based applications, these results should provide generic insights not only into further development of hybrid biotic and abiotic assemblies for artificial photosynthesis but also to those relevant fields.

RESULTS AND DISCUSSION

CdS NR Characterization. The CdS NRs used in the present study were synthesized in an organic solvent [octadecene (ODE)] following previously reported procedures.[31] The transmission electron microscopy (TEM) images of the resulting NRs show an average diameter of 3.4 ± 0.7 nm and a length of 68.3 ± 14.8 nm (Figures 1A and S1). These NRs possess a small spherical bulb region (∼20%) close to the tip (Figure S2) because of the isotropic growth of CdS around the seeds in addition to the prevalent anisotropic growth along the [0001] crystal axis at high temperature.[21,31,32] Ligand exchanges were conducted to transfer the as-synthesized CdS NRs from toluene (∼nmol) to water by vigorously mixing

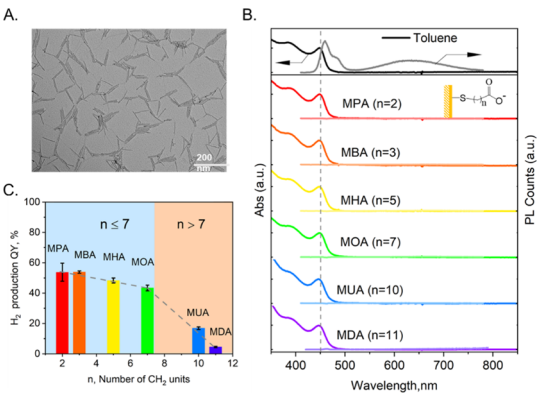

Figure 1. Light to H_2 generation QYs of the CdS NR/PDQ^{2+}/[NiFe]-H_2ase system. (A) TEM of NRs used in the present study. (B) UV−vis absorption and PL spectra of CdS NRs as-synthesized (dispersed in toluene) and capped with mercaptocarboxylate ligands of varying lengths (dispersed in water). Inset: the general chemical structure of the mercaptocarboxylate ligands used herein. n represents the number of $-CH_2-$ units in the alkyl chain. (C) Averaged H_2 production QYs for CdS NR/PDQ^{2+}/NiFe-H_2ase assemblies in the first 30 min under 405 nm LED light illumination (4.26 mW, see Section S1c for details).

https://dx.doi.org/10.1021/acsami.0c07820
ACS Appl. Mater. Interfaces XXXX, XXX, XXX−XXX

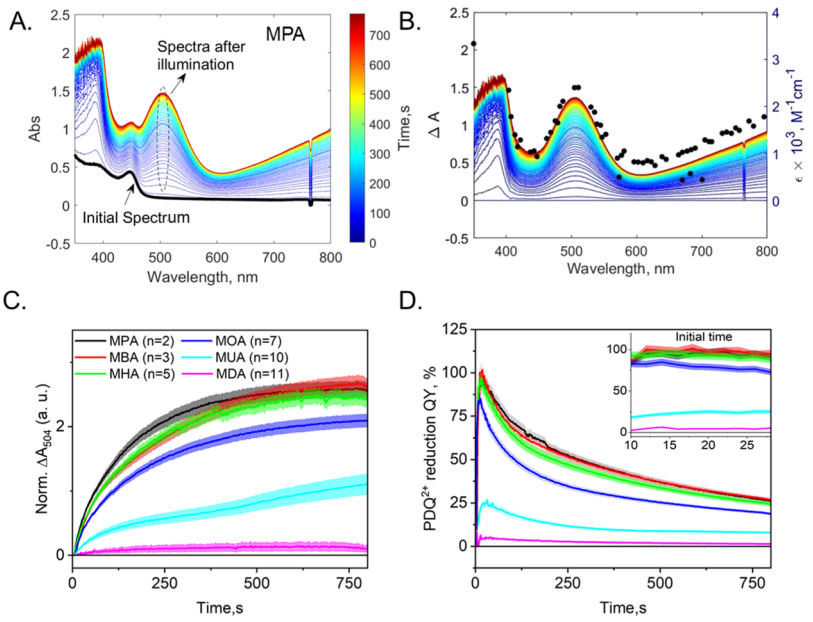

Figure 2. Steady-state spectroscopic characterization of the QYs of redox-mediator photoreduction (step 1 in Scheme 1B) under continuous illumination. (A) Absorption spectra changes of a CdS NR/MPA sample after continuous illumination. Electrolyte composition: 14.5 mM PDQ^{2+}, 50 mM L-cysteine, pH = 6.8 (25 mM phosphate buffer) in deoxygenated solution. Illumination condition: 405 nm LED (4.26 mW). Data for other samples are similar and shown in Figure S5. (B) Absorbance difference spectra (after−before illumination) of the CdS NR/MPA sample shown in panel a (solid lines, left axis) and the extinction coefficient spectra of $PDQ^{+\bullet}$ (dotted line, right axis). (C) Kinetics traces of $PDQ^{+\bullet}$ formation for all CdS NR samples monitored at the peak of $PDQ^{+\bullet}$ absorption at 504 nm, where the ΔA amplitude has been normalized by the absorptivity of different samples at the illumination wavelength (405 nm). (D) Calculated internal QYs of $PDQ^{+\bullet}$ photoreduction as a function of illumination time, which accounts for the light screening effects of the generated $PDQ^{+\bullet}$. The color code is the same as Figure 3C. Inset: the zoomed-in PDQ^{2+} reduction efficiency for the first 30 s.

them with a series of mercaptocarboxylate ligands of the form $HS-(CH_2)_n-COO^-$ (10^4–10^5 nmol) in 0.1 M KOH water solution, with n varying from 2 to 11 (abbreviation shown in Figure 1B). The −SH moiety of mercaptocarboxylate ligands has been previously shown to bind to the surface Cd^{2+} much stronger than the intrinsic phosphate ligands (trioctylphosphine oxide) on the CdS NR surface, with the binding energies reported to be 1283 and 313.6 kJ/mol, respectively.[33] Furthermore, because of the large excess of mercaptocarboxylate ligands (>1000-fold) applied in the ligand exchange reaction, it is assumed below that all intrinsic ligands are displaced from the surface, and the NR surface after the ligand exchange process is covered dominantly by the mercaptocarboxylate ligands. Under the neutral or basic condition, the −COOH moiety of the mercaptocarboxylate ligands is deprotonated,[12] and the resulting negative charge provides the electrostatic interaction for the stabilization of the NRs in water (stable for months). Figure 1B shows the UV−vis absorption and photoluminescence (PL) spectra of the samples before and after ligand exchange. The as-synthesized CdS NRs in toluene show a characteristic band-edge exciton absorption peak at 455 nm and a red-shifted band-edge exciton emission at 459 nm (with a shoulder at 482 nm from the bulb region[31]) and a broad trap-related emission centered at 630 nm.[34] After ligand exchange, the absorption spectra of all the CdS NR samples capped by mercaptocarboxylate ligands in water show negligible changes compared to that in the organic phase, whereas their PL spectra show pronounced quenching of both the band-edge and trap emissions, which has been attributed to ultrafast hole transfer to surface thiolate ligands.[35]

In the following sections, we first report the dependence of the steady-state H_2 production and photoreduction of PDQ^{2+} molecules on the length of the capping ligands in our hybrid system. The results points out different ligand length-dependent H_2 production behavior as those previously reported in the direct ET based hybrid system as previously reported.[12] We then provide a detailed analysis of the efficiency limiting step of the system. After that, we conduct detailed interfacial ET studies to understand the mechanism of such distinct behavior.

Ligand Length-Dependent Light to H_2 Generation Quantum Efficiency. We measured the light-driven H_2 generation quantum yield (QY) of the CdS NR/PDQ^{2+}/[NiFe]-H_2ase systems with different ligands at pH = 6.8, using LED illumination (405 nm, 4.26 mW) and L-cysteine (50 mM, E^0 = ~0.02 V vs NHE at pH ~ 7[36]) as a sacrificial electron donor (see the Experimental Section). Because two electrons are required to produce one H_2 molecule, QY is defined as twice the ratio between the amount of generated H_2 (n_{H_2}) and the absorbed photons (n_{photon}) by the CdS NR (eq 1).

$$QY = \frac{2 \times n_{H_2}}{n_{photon}} \times 100\% \quad (1)$$

Figure 1C shows the average QYs measured within the first 30 min of LED illumination of the CdS NR/PDQ^{2+}/[NiFe]-H_2ase systems as a function of the ligand length of the NRs. These reported QYs do not account for light scattering loss and light absorption of the steady-state $PDQ^{+\bullet}$ generated during the H_2 production (see below) and therefore represent the lower limit of the QYs. The hybrid system of CdS NRs with the shortest ligand length, MPA, show a QY as high as 54 ± 6%, close to previous QY obtained using a CdSe/CdS dot-in-rod structure.[16] Further inspection of the ligand length-

https://dx.doi.org/10.1021/acsami.0c07820
ACS Appl. Mater. Interfaces XXXX, XXX, XXX−XXX

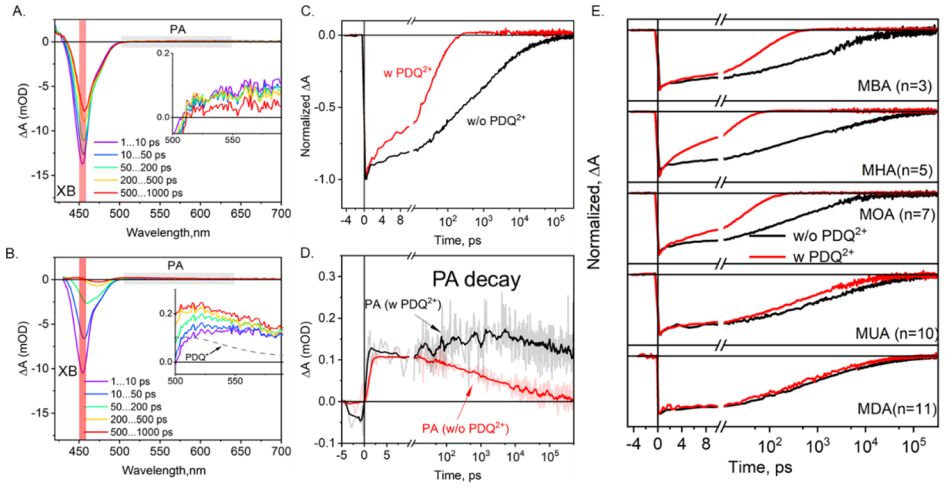

Figure 3. TA spectroscopic measurement of apparent ET rate and kinetics. Averaged TA spectra for CdS NR/MPA in water without (A) and with (B) addition of PDQ^{2+} at indicated delay time windows. Inset in (A,B): the zoom-in spectral region between 500 and 575 nm. Comparison of decay kinetics of XB at 464 nm (C) and PA at 500 nm (D) for CdS NR/MPA samples with and without PDQ^{2+}. (E) Comparison of XB decay kinetics of CdS NR/MBA, CdS NR/MHA, CdS NR/MOA, CdS NR/MUA, and CdS NR/MDA at 464 nm with and without the addition of PDQ^{2+}.

dependent QYs indicates the existence of two domains of ligand length-dependent H_2 production (Figure 1C). For short ligands (n = 2 to 7), an increase of the ligand length results in only a minor decrease of QYs from 54 ± 6 to 43 ± 2%. However, a further increase of the ligand length from n = 7 to 11 results in a large drop of the QY to only 16 ± 1 and 4 ± 0.4% for n = 10 and 11, respectively. These results are in remarkable contrast with previously reported results for a direct contact CdS NR/H_2ase system, where the QY drops by more than 90% from n = 2 to 7.[12]

Ligand Length-Dependent Steady-State PDQ^{2+} Photoreduction Efficiency. To better understand the above-observed trend of H_2 production QYs, we quantify the QYs of the first step (Scheme 1B), that is, the photoreduction of PDQ^{2+} to $PDQ^{+\bullet}$, using systems with only CdS NRs, PDQ^{2+}, and hole scavengers under continuous 405 nm LED illumination and by monitoring the distinct spectral feature of $PDQ^{+\bullet}$. Figure 2A shows an example absorption spectral evolution using the CdS NR/MPA sample, with the data for other samples shown in Figure S4. Upon illumination, a gradual increase of new absorption features appears across the UV−vis range. The resulting difference absorption spectra (Figure 2B) show characteristic peaks at 386 and 504 nm and a broad feature beyond 600 nm. These features agree well with the previously measured absorption spectrum of $PDQ^{+\bullet}$ (overlaid dot symbols in Figure 2B[22]), confirming the photoreduction of PDQ^{2+} to $PDQ^{+\bullet}$ by the CdS NRs. To account for the light absorptance difference of different CdS NR samples, all the difference spectra are further normalized by the absorptivity of the corresponding NRs at 405 nm before illumination. Figure 2C shows the normalized kinetic traces of the different absorption at 504 nm as a function of illumination time for different samples. All these traces show that the generated $PDQ^{+\bullet}$ concentration reaches a plateau after ~10^3 s, with the plateau amounts of the photogenerated $PDQ^{+\bullet}$ following the order of MPA ≈ MBA ≈ MHA > MOA ≫ MUA > MDA, in qualitative agreement with the trend observed for overall H_2 production QYs (Figure 1C). This plateau behavior is partially caused by the light screening of the generated $PDQ^{+\bullet}$, which is evidenced by the increase of their light absorption at 400 nm from 0 to 0.7 OD (at ~750 s) (Figure 2A). To account for the light-screening effect, the internal QYs of PDQ^{2+} photoreduction are calculated by dividing the amount of generated $PDQ^{+\bullet}$ by the absorbed photons by the NRs at a given time (details shown in the Note S2a) and shown in Figure 2D. As shown in the inset of Figure 2D, the initial internal QYs are close to 100% in NRs with MPA (~100%), MBA (~100%), MHA (~100%), and MOA (~85%) but are much smaller for those with MUA (20%) and MDA (4%). However, with prolonged illumination time, the $PDQ^{+\bullet}$ generation QYs decrease for all samples. For example, the internal QY of the CdS NR/MPA sample decreases from the initial ~100% to only ~40% at 750 s. During this period, the NR concentrations remain the same as before illumination; the photogenerated $PDQ^{+\bullet}$ is calculated to be ~0.2−5% of the total initial concentration of PDQ^{2+}, while the sacrificial hole acceptors (50 mM) are still in great excess for all samples. As such, the decrease in the internal QYs is not caused by the decrease of these three reagents. Control experiments show that, after turning the light off to allow the complete decay of $PDQ^{+\bullet}$ and re-illuminating the systems, similar growth kinetics and initial internal QYs (approximate ~80% of the initial value) are observed (Figure S5). This result suggests that the abovementioned decrease of the internal generation QYs of $PDQ^{+\bullet}$ is likely caused by the accumulation of $PDQ^{+\bullet}$, which can be expected to increase the bimolecular charge recombination loss between the $PDQ^{+\bullet}$ and photogenerated holes in CdS and/or increase the self-decomposition (Figure S5, with a lifetime of 10−100 s). These abovementioned discussion reveals that the accumulation of $PDQ^{+\bullet}$ decreases the external QYs of the mediator-based system by not only light-screening effects but also the increased recombination. Therefore, further optimization of the system should be aimed to reduce the accumulation of $PDQ^{+\bullet}$ by optimizing the concentration of various components or utilize different redox mediators. It should be noted that, in the presence of [NiFe]-H_2ase, ET from $PDQ^{+\bullet}$ to [NiFe]-H_2ase should alleviate the extent of $PDQ^{+\bullet}$ accumulation, thus reducing the correspondent recombination loss. However, as shown in Figure S6, this ET rate is not fast enough to completely eliminate the

https://dx.doi.org/10.1021/acsami.0c07820
ACS Appl. Mater. Interfaces XXXX, XXX, XXX−XXX

accumulation of $PDQ^{+\bullet}$, with minor accumulation of $PDQ^{+\bullet}$ still observable in the CdS NR/PDQ^{2+}/[NiFe]-H_2ase system as well.

Ligand Length-Dependent Apparent ET Transfer Rate and Efficiency from NR to PDQ^{2+}. The above-mentioned PDQ^{2+} photoreduction QYs under continuous illumination depend on both the QYs of initial ET from the NR to PDQ^{2+} and the subsequent charge recombination between $PDQ^{+\bullet}$ and the photogenerated holes. To directly measure the QYs of initial ET from the NR to PDQ^{2+}, we employed transient absorption (TA) spectroscopy ranging from fs to μs to investigate the ET kinetics of samples consisted of only CdS NRs and PDQ^{2+}. TA measurements were all conducted under low excitation fluence to ensure single exciton excitation conditions (Figure S7). Figure 3A shows the average TA spectra of MPA-capped CdS NRs in the absence of PDQ^{2+} (referred to as CdS NR/MPA) at indicated delay time windows after 400 nm excitation. The TA spectra for other samples show similar features and are, therefore, omitted for clarity. These TA spectra show a major bleach band at 455 nm (XB) and a shoulder at 460 nm, which have been previously assigned to the state-filling effects of the band-edge exciton of the NRs and bulb regions, respectively (Figure S8).[31] The TA spectra also show a broad featureless photoinduced absorption (PA) extended from 520 nm to 700 nm (inset of Figure 3A), which has been previously attributed to the holes in the CdS NRs.[34] Because only small portions of NRs contain a bulb region and their volume and surface areas are much smaller compared to the rod region,[37] below, we used the XB of the rod to follow the conduction band electron kinetics (Figure 3C).[38] Also, the decay of XB cannot be fitted with a single exponential function and the detailed physical model of the underlying kinetics remains unclear; for simplicity, we use the halftime of XB decay to quantify its decay time constant.[39]

In the absence of PDQ^{2+}, the XB decay, representing the intrinsic recombination and/or trapping of the photogenerated electrons in CdS NR, shows a halftime, $t_{1/2,}$ in the range of 0.4−0.9 μs for all CdS NR samples without a clear length-dependent trend (Figure 3C,E). In the presence of PDQ^{2+}, the TA spectra (Figure 3B) show that the XB decay accelerates dramatically, with $t_{1/2}$ shortened to 25 ± 2 ps in CdS NR/MPA (Figure 3C); furthermore, the TA spectra show a simultaneous formation of a positive peak centered around 520 nm (inset in Figure 3B), consistent with the absorption spectrum of $PDQ^{+\bullet}$ (gray dashed line). The growth of the $PDQ^{+\bullet}$ absorption can also be seen in the comparison of kinetics at 500 nm of CdS NR/MPA samples with and without PDQ^{2+} (Figure 3D). These spectral and kinetics features confirm ET from the CdS NR/MPA to PDQ^{2+} and the formation of $PDQ^{+\bullet}$, similar to the previous observation in a CdS quantum dot/PDQ^{2+} system.[40] Control experiments (Figure S9) show that the decay of XB changes negligibly from that of free NRs when directly binding the [NiFe]-H_2ase to the CdS NR, indicating insignificant direct ET from the CdS NR to the [NiFe]-H_2ase and the essential role of the mediator described in Scheme 1 as reported previously.[16] Figure 3E further compares the XB decays of other samples in the absence and presence of PDQ^{2+}, with their decay halftimes summarized in Table 1. The results show a similar extent of acceleration of the XB decay in the presence of PDQ^{2+} for NRs capped with MPA, MBA, MHA, and MOA ligands, indicating similar apparent ET rates from the NR to PDQ^{2+} in these samples. However, the apparent ET rates in NRs capped with MUA and MDA are significantly slower, with only a minor acceleration of XB decay in the presence of PDQ^{2+}. With these measured decay half-times with ($t_{1/2,\ PDQ}$) and without ($t_{1/2}$) PDQ^{2+}, the ET QYs can also be calculated using eq 2.

Table 1. Efficiency of ET to PDQ^{2+} of NR/Ligand Assemblies

	$t_{1/2}$ (ps)[a]	$t_{1/2,PDQ}$ (ps)[a]	ET efficiency (%)[b]
MPA	484 ± 86	25 ± 2	95 ± 1
MBA	596 ± 26	33 ± 7	94 ± 1
MHA	396 ± 26	13 ± 4	97 ± 1
MOA	357 ± 133	20 ± 1	94 ± 2
MUA	879 ± 69	379 ± 31	56 ± 7
MDA	694 ± 10	423 ± 20	39 ± 5

[a] $t_{1/2}$ and $t_{1/2,PDQ}$ stand for the XB decay halftime of NRs, capped with different mercaptocarboxylate ligands, in the absence and presence of PDQ^{2+} molecules, respectively (Figure 3C,E). [b] represents the calculated ET efficiency of electrons in the NR to PDQ^{2+} according to eq 2.

$$QY = \frac{k_{ET}}{k_{ET} + k_{int}} = 1 - \frac{t_{1/2,PDQ}}{t_{1/2}} \quad (2)$$

The results (Table 1) indicate a near-unity ET QY in NRs capped with MPA (95 ± 1%), MBA (94 ± 1%), MHA (97 ± 1%), and MOA (94 ± 2%). However, the QYs for NRs capped by the MUA and MDA ligands are much smaller, around 56 ± 7 and 39 ± 5%, respectively. It should be noted that although a more advanced model for estimating ET QYs from nonexponential kinetics has been reported,[21] we have adopted the simple half-time method (eq 2) to capture the qualitative trend of ligand length dependence.

Figure 4 summarizes the above-characterized ligand-length dependent QYs of H_2 generation (Figure 1C), PDQ^{2+} photoreduction (Figure 2D), and ET (Table 1). These results all show the existence of a crucial alkyl chain length between n = 7 and 10, above which the QYs for ET, PDQ^{2+} photoreduction, and H_2 production all drop dramatically. Though ET rates from NRs of various ligands to many acceptors have been reported,[11,12] the above result represents the first report on the abrupt change of ET behavior caused by the ligand length. In the next sections, we further investigate

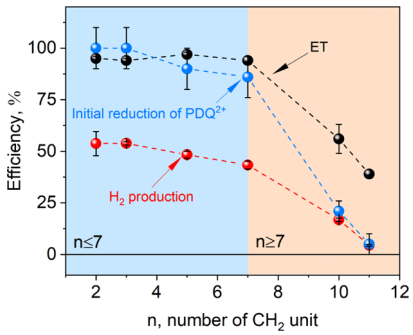

Figure 4. Comparison between the QYs of steady-state H_2 production, steady-state PDQ^{2+} photoreduction, and transient ET from the CdS NR to PDQ^{2+} measured using NRs capped with mercaptocarboxylate ligands with a varying number of CH_2 units in the alkyl chain.

https://dx.doi.org/10.1021/acsami.0c07820
ACS Appl. Mater. Interfaces XXXX, XXX, XXX−XXX

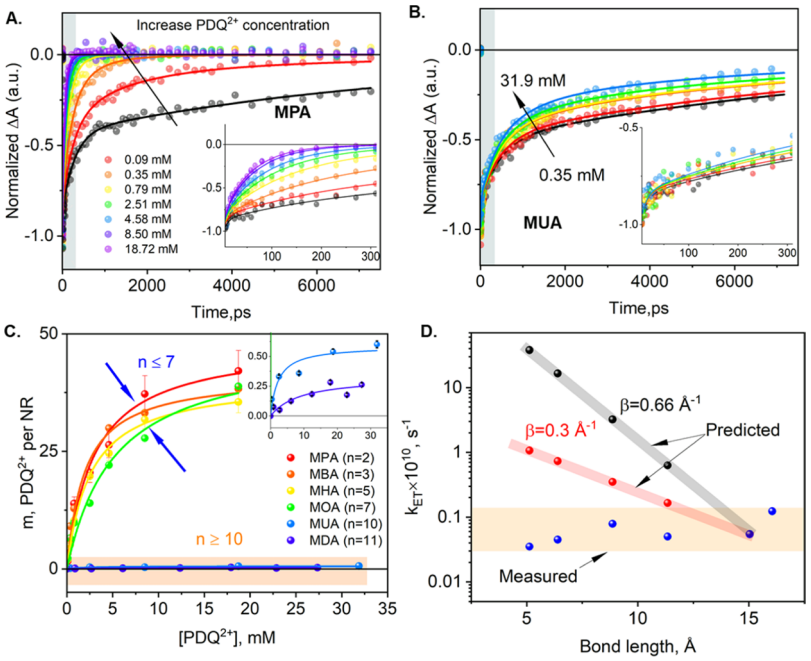

Figure 5. Ligand length-dependent intrinsic ET rates and mediator adsorption sites on NR surfaces. Dependence of XB decay (colored dots) on PDQ^{2+} concentration for (A) CdS NR/MPA and (B) CdS/NR/MUA. Data without PDQ^{2+} are shown as gray dots. The solid lines are the global fits of these curves according to the model (eq 4) described in the main text. Data for other samples are shown in Figure S10. (C) Extracted number of surface adsorbates (m) per NR as a function of solution PDQ^{2+} concentration for all CdS NR samples. (D) Intrinsic ET rate constants in 1:1 NR/adsorbate complexes for all CdS NR samples (blue dots), with the error range estimated to be 10%. The red dots and black dots are the predicted rate constants according to eq 5, with β of 0.3 and 0.66 $Å^{-1}$, respectively, from previous reports.[11,12] The marked areas are shown for visualization.

the mechanisms for the existence of these two domains of ET behaviors.

Ligand Length-Dependent Intrinsic Rate ET Rate Constants and Surface Adsorption. In NR/acceptor assemblies, the apparent ET rate (k_{ET}) increases with the number of acceptors on the NR (n_a), that is, $k_{ET} = n_a \times k_{int}$, where k_{int} is the intrinsic ET rates to one adsorbed acceptor. Thus, the observed ligand-dependent apparent ET rate might be caused by a change in k_{int} and/or n_a. To determine which is the case, we studied the dependence of apparent ET rate as a function of total PDQ^{2+} concentration for all CdS NRs capped with different mercaptocarboxylate ligands. Figure 5A,B shows the XB decay curves of CdS NR/MPA and CdS NR/MUA samples as a function of PDQ^{2+} concentration (data for other samples in Figure S10). In both samples, an increase in PDQ^{2+} concentration leads to the gradual acceleration of the XB decay—i.e., a faster apparent ET from CdS NRs to PDQ^{2+}—because of more adsorbed PDQ^{2+} molecules. However, the extent of acceleration is noticeably much smaller for the CdS NR/MUA samples.

We analyze the concentration-dependent ET kinetics by following a previously well-developed model.[41−44] In this model, it is assumed that the number of acceptors on the nanocrystal surface follows a Poisson distribution; if the exciton bleach of the NR follows a multiexponential decay (eq 3) with amplitudes (time constants) of A_i (τ_i), the exciton bleach of a NR/acceptor sample with m averaged number of acceptor per NR can be expressed as eq 4.[45]

$$\Delta A_0(t) = \sum_i A_i \exp\left(-\frac{t}{\tau_i}\right) \tag{3}$$

$$\Delta A(t, m) = \exp\{-m(1 - \exp(-k_{int}t))\} \times \sum_i A_i \exp\left(-\frac{t}{\tau_i}\right) \tag{4}$$

In a typical fitting process, we start by fitting the intrinsic decays of XB decay for the CdS NR samples capped with different ligands (gray dots in Figures 5a,b and S11) with three-exponential decay according to eq 3 to obtain the values of A_i and τ_i (fits shown as black lines and fitting parameters summarized in Tables S1−S6). The PDQ^{2+} concentration-dependent ET kinetics can be then fitted globally with only k_{int} (concentration-independent) and m (concentration-dependent) as free parameters. As shown in Figure 5A,B, the experimentally observed data can be well fit by this model. The intrinsic rate constants, k_{int}, extracted from the fits are surprisingly similar for all CdS NR/mercaptocarboxylate samples, falling within the range of 10^8−10^9 s^{-1} (Figure 5D). Figure 5C shows a plot of the extracted m value as a function of [PDQ^{2+}], where a clear Langmuir adsorption isotherm behavior is observed for all cases. These isotherm curves are then fitted to obtain binding constants and the saturated surface coverage, which are summarized in Table S7. The results show that the binding constants of all the samples capped with different mercaptocarboxylate ligands show only small scattering between 0.1 and 0.6 mM^{-1}. These values are also consistent with previously reported binding constants of PDQ^{2+} (0.32 mM^{-1}) onto a dot-in-rod CdS@CdSe NRs determined by photoluminescent quenching[16] and for other QD-organic molecule complexes.[41] Such bindings have been suggested to arise from the direct electrostatic interaction between the bipyridine core and the nanocrystal surface.[46,47]

https://dx.doi.org/10.1021/acsami.0c07820
ACS Appl. Mater. Interfaces XXXX, XXX, XXX−XXX

Remarkably, the saturated number of surface-adsorbed PDQ^{2+} are similar for NRs with MPA, MBA, MHA, and MOA, all within 40−50. However, the saturated coverage for NRs with MUA and MDA is only 0.6 ± 0.1 and 0.3 ± 0.1, respectively. Thus, for CdS NRs with different mercaptocarboxylate ligands, the binding constant and ET rate between the NR and PDQ^{2+} are independent of the ligand length, indicating a similar PDQ^{2+} binding mechanism and electronic coupling strength with the NRs. However, there is an abrupt decrease of the number of surface adsorption sites on the NR surface for longer chain ligands ($n > \sim 7$), which decreases the number of adsorbates and the apparent ET rates and accounts for the abovementioned distinct H_2 production trend.

Proposed Model for the Abrupt Ligand Length-Dependent ET Behavior. The ligand length dependence of ET from CdS NRs to PDQ^{2+} is in strong contrast with previous findings of direct ET from CdS NRs to hydrogenase enzymes without a mediator.[12] In that system, k_{int} has been reported to decrease with the ligand length (d) with an attenuation factor, β, of 0.66 $Å^{-1}$ as described by eq 5.[12]

$$k \propto k_0 \exp(-\beta d) \tag{5}$$

Another study on the ligand length-dependent ET rates also reported a β value of 0.3 $Å^{-1}$ using similar mercaptocarboxylate ligands between CdSe quantum dots and a polyviologen acceptor.[11] Both these studies used bulky acceptors, for example, an enzyme[12] or a polymer,[11] that are too large to penetrate the capping ligands on the NR surface. In such cases, ET occurs by tunneling through the ligand layer, giving rise to the exponential decrease of coupling strength with distance. As shown in Figure 5D, using β values of 0.3 and 0.66 $Å^{-1}$, k_{int} is predicted to increase from 10^8 to 10^{11} s^{-1} from the MUA to MPA ligand. Clearly, the observed results cannot be explained by the length-dependent ET tunneling behavior.

On the other hand, it is well known that alkanethiols form self-assembled monolayers (SAMs) on both flat Au surfaces[48] and Au nanoparticle surfaces (d = 30 Å),[49] stabilized by interchain van der Waals interactions. The SAMs can undergo a phase transition from the disordered "liquid" phase to ordered "crystalline" (or "gel") phase when the number of the $-(CH_2)_n-$ units in the alkanethiols increases.[48] These SAM phases have different ligand packing densities,[48] ligand layer thickness, and water permeability.[50] It has also been reported that changing the terminal groups from $-CH_3$ to $-COOH$ has little impact on the structural order but may introduce gauche defects on the SAMs.[51] The typical number of the $-(CH_2)_n-$ unit in the alkanethiol ligand that triggers the "liquid" to "crystalline" phase transition on gold was characterized to be between n = 7 and 10 at room temperature,[48,52,53] in remarkable agreement with the chain length for the abrupt decreases of adsorption sites observed in the present study. Therefore, we hypothesize a mechanism involving the self-assembly of the alkanethiol on the surface of CdS NRs which may account for the abovementioned results, as shown in Scheme 2. In this model, when the capping ligand is short (n < 7), the SAM layer on CdS NRs is disordered, allowing high permeability of small molecules, for example, PDQ^{2+} in the present study, into the CdS NR surface (Scheme 2A). As a result, the ET QY is almost unity and independent of the alkyl chain length. However, when the capping ligand length is long (n > 9), the stronger lateral van der Waals interactions between the nearby mercaptocarboxylate ligands leads to (partial) crystallization of the ligands on the NR surface. This "phase transition" results in the formation of strong hydrophobic chain domains to reduce the surface accessibility of the NR by small molecules, which accounts for the sudden drop in the surface coverage of mediators (Scheme 2B).

Scheme 2. Proposed Mechanism for the Two Domains of Ligand Length-dependent ET; (A) When n is between 2 and 7, the Ligands on the Surface are Highly Disordered, Allowing the Free Diffusion and Adsorption of Small Molecules to the Surface and Conduct ET; As Such, the ET Efficiency Is Not Very Sensitive to the Ligand Length; (B) When n is Larger than 10, the Interchain van der Waals Interaction of the Ligands Results in the (Partial) Crystallization of the Ligand; As Such, the Amount of Surface-Adsorbed Molecules is Decreased Significantly, Resulting in an Abrupt Change of the ET

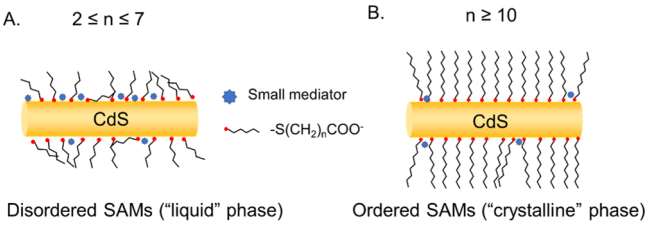

To provide further evidence for the proposed ligand length-dependent phase transition, we compare the order of SAM layers of 1-butanethiol [$CH_3(CH_2)_3SH$, named as BT below] and 1-dodecanethiol [$CH_3(CH_2)_{11}SH$, named as DT below] molecules on the Au surface by using SFG spectroscopy.[54−58] These two molecules were chosen to represent the MPA (n = 3) and MDA (n = 11) molecules by replacing the terminal $-COOH$ unit by the $-CH_3$ unit, because the ratio of the $-CH_3$ and the $-CH_2-$ unit in SFG is a well-known experimental handle to determine the ordering of the methylene units in alkanethiol molecules.[58,59] The Au surface is chosen because of the strong binding of thiol groups on the gold surface[54,55] and the experimental challenges of directly measuring SFG on nanocrystal surfaces.[59] Because the lattice constants (a = 4.160 and c = 6.756)[60] of the wurtzite CdS crystals examined here are similar to that of fcc Au (4.065 Å), these results, although achieved on the Au surface, should still provide valuable insights toward the packing of alkanethiol molecules on the CdS crystal surface. In an ideal all-trans configuration, the $-CH_2-$ unit in the alkanethiol molecules is known to have no SFG signals response because of its centrosymmetric alignment and the vanishing χ^2 term in nonlinear optical processes.[58] On the other hand, in a disorder ligand system, the presence of gauche defects in the ligand layer resulting in the $-CH_2-$ stretching is no longer in a centrosymmetric environment, enabling in the appearance of the $-CH_2-$ signals together with the $-CH_3$ signal in the SFG data. Indeed, as shown in Figure S11, the asymmetric stretching modes of both $-CH_2-$ and $-CH_3$ signals for the BT-derived surface are observed, indicating the disordering of alkanethiol ligands with n = 3; on the other hand, for DT-derived Au surface, only the asymmetric $-CH_3$ stretching signals are observed, indicating that the all-trans ordering of the $-CH_2-$ chain for the n = 11 cases, in agreement with previous results.[57,59] These results show that an increase of alkyl chain length from n = 3 to 11 can indeed result in the clear change of the packing of the alkanethiol molecules.

To provide direct evidence that such configuration order change of ligands can also exist on the nanocrystals surface, we

https://dx.doi.org/10.1021/acsami.0c07820
ACS Appl. Mater. Interfaces XXXX, XXX, XXX−XXX

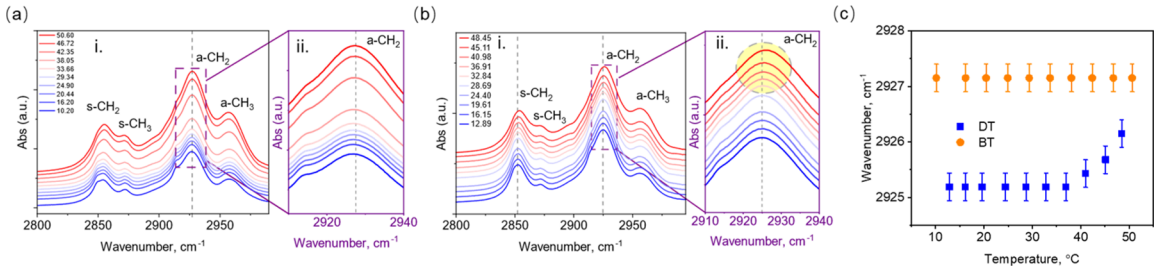

Figure 6. Temperature-dependent IR absorption spectral changes of CdS NR dispersed in $CDCl_3$ when capped with (a) BT, $CH_3(CH_2)_3SH$, and (b) DT, $CH_3(CH_2)_{11}SH$. The temperature was controlled between 10 and 50 °C, limited by the volatile nature of $CDCl_3$. Here, the a-CH_2 (a-CH_3) and s-CH_2 (s-CH_3) symbols represent the asymmetric and symmetric stretching of the $-CH_2-$ ($-CH_3$) unit in the corresponding alkanethiol molecules on the CdS surface, respectively. The subpanel (i,ii) represents the original measured spectra and the zoom-in a-CH_2 spectral region, respectively. (c) Dependence of the extracted a-CH_2 peak position in BT- (a) and DT- (b) CdS NR on the applied temperatures. The small red-shift that is observed in the case of DT-CdS surface indicates an "order" to "disorder" transition of the alkanethiol on the CdS NR surface. The error in the peak position is estimated to be ±0.25 cm^{-1}.

measured the temperature-dependent IR spectra of BT and DT capped CdS NR dispersed in $CDCl_3$ (boiling point: 61.2 °C), as shown in Figure 6a,b, respectively. Previous studies of alkanethiols on planar Au surface demonstrate that the packing order change of the alkanethiols is sensitive to its packing order, where the "crystalline" to "liquid" phase of these ligands can result in a redshift of the asymmetric stretching frequency of the methylene unit (a-CH_2) from 2918 to 2921 cm^{-1}.[51] As shown in Figure 6a, for the BT-capped nanocrystals, the a-CH_2 IR peak locates approximately at 2927.2 ± 0.25 cm^{-1} and demonstrates negligible shifts from 12.89 to 50.6 °C [Figure 6a(ii),c]. For the DT capped samples, at the low-temperature range (12−40 °C), there is a negligible spectral shift, 2925.2 ± 0.25 cm^{-1} [Figure 6b(ii),c]; but further temperature increase from ∼40.98 to 48.45 °C leads to a redshift of the a-CH_2 peak from 2925.2 ± 0.25 to 2926.2 ± 0.25 cm^{-1}, with the latter frequency closer to the a-CH_2 in BT-capped nanocrystals (2927.2 ± 0.25 cm^{-1}). These results, therefore, indicate that a similar phase transition exists at ∼40 °C for DT (n = 11) on the CdS NR surface as on the gold surface as well. As such, at the room temperature, the ligand configurations in the DT- and BT-capped nanocrystals are likely in "crystalline" and "liquid" phases, respectively. This finding is also consistent with a recent report by Alivisatos and coworkers[61] that demonstrates the presence of "order" to "disorder" transition of aliphatic chains on the CdSe/CdS core−shell quantum dot surface and its effect on their PL quantum efficiencies. The direct measurement of this small (1−2 cm^{-1}) temperature-dependent peak shift of mercaptocarboxylate-capped NRs in water has been hindered because of the overlap of $-CH_2-$ stretching modes with the strong absorption of water and the broadening of this transition. It should be noted that the ionic interaction between the carboxylate terminal of the ligand used in the present study may introduce additional complications toward the ligand interaction than those probed herein with the BT- and DT-derived surface. Nevertheless, these above spectroscopic evidence of SAM on nanocrystals and planar Au surface[48,52,53] provide strong evidence for the existence of length-dependent ligand configuration change on CdS NR surfaces, agreeing well with the abrupt ligand length dependence in the efficiencies of ET, steady-state PDQ^{2+} reduction, and H_2 production discussed above (Figure 4).

Our result demonstrates that the length-dependent surface ligand order−disorder transition can regulate ET between QDs and molecular acceptors and significantly affect the H_2 production efficiency of mediator-based hybrid abiotic−biotic systems. This concept is also expected to be applicable for other nanomaterial-acceptor assemblies, where intimate interaction of nanocrystal, surface ligands, and acceptor molecules is required. In other photocatalytic applications of nanocrystals,[5,6] the chemical transformation of small organic molecules into valuable products requires the adsorption of small molecules on the surface for efficient electron/hole transfer processes. For the emerging nanocrystal triplet sensitization/up-conversion system,[2−4] the efficiency of energy transfer between the nanocrystal and triplet acceptor is distance-dependent[62,63] and may also be modulated by the ligand order. Further studies, which can unambiguously illustrate the detailed microscopic structure of the ligand layers[36] and its dependence on the curvature and exposed facet of the nanocrystals will be of crucial importance, although they are still major experimental challenges.

CONCLUSIONS

In summary, the present study investigates the ligand length-dependent H_2 production in a state-of-art mediator-based abiotic (CdS NR) and biotic ([NiFe]-H_2ase) hybrid system for light-driven H_2 production. The H_2 production QY reaches 54 ± 6% under 405 nm LED illumination for CdS NRs capped with the shortest ligand, MPA. Detailed studies reveal that the initial photoreduction efficiency of the mediator is close to unity. However, the accumulation of $PDQ^{+\bullet}$ reduces the efficiency of the system by both a light screening effect and an accelerated recombination loss. These results indicate that further optimization of the mediators to reduce the impact of this accumulation is critical to improve the efficiency of these mediator-based systems. More importantly, the QYs of the steady-state H_2 production, steady-state PDQ^{2+} photoreduction and initial ET show very little ligand length dependence at n < 7 and decreases rapidly at n = 10 and 11. A detailed study of the PDQ^{2+} concentration dependence of the apparent ET rate reveals that the main difference of ET rates is caused by a large decrease of accessible surface adsorption sites in NRs with long capping ligands. We propose that there exists a disordered "liquid" to a more ordered "crystalline" phase transition of mercaptocarboxylate ligands between n = 7 and 10, which regulates the accessibility of the small electron acceptors to the NR surface. This model is further supported by the SFG and temperature-dependent IR measurements. These results demonstrate that surface capping ligands of nanocrystals can be more than a simple barrier for electron

https://dx.doi.org/10.1021/acsami.0c07820
ACS Appl. Mater. Interfaces XXXX, XXX, XXX−XXX

tunneling between nanocrystals and mediators. The microscopic structure of the capping ligands, an indispensable part of nanocrystals, should be further utilized as an additional design parameter to construct hybrid abiotic and biotic materials with more sophisticated and improved functions.

EXPERIMENTAL SECTION

Reagents. All chemicals were purchased from Sigma-Aldrich and used without further purification unless otherwise mentioned. These include cadmium oxide (99.998%), trioctylphosphine oxide (99%), trioctylphosphine (97%), tributylphosphine (97%), ODE (technical grade, 90%), oleic acid (technical grade, 90%), sulfur (99.98%), 3-mercaptopropionic acid (≥99%), 4-mercaptobutyric acid (Aldrich CPR), 6-mercaptohexanoic acid (90%), 8-mercaptooctanoic acid (95%), 11-mercaptoundecanoic acid (95%), and 12-mercaptododecanoic acid (96%). *N*-Hexylphosphonic acid (95%) and octadecylphosphonic (>99%) were purchased from PCI synthesis.

NR Synthesis and Ligand Exchange. All the chemicals are used as received without further purification. The synthesis of CdS NR followed a seeded growth procedure reported in the previous literature with slight modification.[34] For the seed synthesis, 0.077 g of CdO, 0.5 mL of oleic acid, and 15 mL of ODE were first mixed in a 50 mL three-neck flask and degassed under vacuum at 120 °C for 10 min. After that, the solution is further raised to 280 °C and held until the complete solvation of CdO. (Solution turns from a reddish color to transparent). Further, 0.0096 g S in 3 mL ODE is injected into the solution. The reaction was stopped after 30 s of the injection, and an additional 10 mL ODE is injected to stop the reaction. After that, the QD was precipitated by adding ethanol and followed by centrifugation at 5500 rpm for 5 min. The precipitated solid is redispersed in toluene. This washing procedure was repeated a few times.

For the NR synthesis, 0.06 g of CdO, 3 g of trioctylphosphine (TOP), 0.29 g of octadecylphosphonic acid, and 0.08 g of hexylphosphonic acid are degassed under vacuum for 10−20 min at ∼ 150 °C. After that, the solution temperature is raised to 350 °C and waits until the solution turned from a reddish color to transparent, indicating the complete dissolution of CdO. Following that, 1.8 mL of TOP is injected into the solution. After the stabilization of the temperature back to 350 °C. 0.12 g of S in 1.8 mL of TOP mixed with ∼10 nmol CdS seed is quickly injected. The reaction is continued for 8 min. Reactions are stopped by removing the heating mantles, cooled by blow air, and merged into cold water. Products are precipitated by the addition of ethanol and later dissolved into hexane.

For ligand exchange experiments, 2 mL NR in Toluene (∼nmol), 10 μL or (10 mg in case of MUA and MDA) mercaptocarboxylate ligands (10^4 to 10^5 nmol), and 2 mL 0.1 M KOH in water were mixed and stirred overnight.[64] Finally, all the mercaptocarboxylate-capped NRs were precipitated and redissolved in distilled water.

UV−Vis and PL Measurements. All static PL measurements were performed with FluoroMax-3 Spectrofluorometer of HORIBA Scientific. The excitation wavelength is 400 nm for all the samples, and the scan range is from 420 nm to 700 nm. Steady-state UV−vis spectra were recorded on an Aligent spectrometer (G1103A). For the photoreduction measurements, all the solution was first purged throughout with argon. During the photoreduction measurement, the upper part of the solution is illuminated by a 405 nm LED under vigorous stir, while the light absorption of the lower part of the solution is simultaneously monitored at a 2 s intervals using the Ocean optics.

H_2 Production Measurements. For a typical H_2 production measurement, the electrolyte consists of NRs capped with one of the mercaptocarboxylate ligands (the band-edge absorbance is typically controlled to be ∼0.3−0.5), 14.6 mM PDQ, 50 mM L-cysteine, 0.1 μM [NiFe] H_2ase in a pH = 6.8, 25 mM phosphate buffer solution (named as Kpi below). The electrolyte (1.54 mL) was put into a cylindrical polarimeter cell (total volume ∼2.8 mL, Type 32S, Fireflysci) with a septum cap and degassed with argon before the H_2 production experiments for 15 min. During the H_2 production, a 405 nm LED (beam size ∼0.20 cm^2, 4.26 mW) was used as the light source and focused entirely on the samples. The samples were all under vigorous stirring. The H_2 production of the systems is measured by gas chromatography (Agilent 7890B) by sampling the headspace (∼1.26 mL) of the capsulated vials at fixed time intervals, typically every 5 min, and monitored continuously for 1 h. During each sampling, we first injected 100 μL argon into the vial and then took out 100 μL headspace gas in order to maintain the constant volume of the headspace gas. The dilution effect of the injected argon was accounted for during the calculation of the H_2 production efficiency.

Femtosecond TA Spectroscopy. The TA measurements were conducted in a Helios spectrometer (Ultrafast Systems LLC) with pump and probe beams derived from a regenerative amplified Ti: Sapphire laser system (Coherent Legend, 800 nm, 150 fs, 3 mJ/pulse, and 1 kHz repetition rate). The 800 nm fundamentals are split into two parts. One part of the 800 nm output pulse passed through a frequency-doubling BBO crystal and generated the 400 nm excitation beam. Another part of the 800 nm beams was attenuated and focused on a sapphire window for the generation of the white light continuum, with a wavelength range from 420 nm to 800 nm. The white light was split into both a reference and a probe beam by using a beam splitter. The probe beam was focused with an Al parabolic reflector onto the sample. The reference and probe beams were focused into a fiber optics-coupled multichannel spectrometer with complementary metal-oxide-semiconductor (CMOS) sensors and detected at a frequency of 1 kHz. During the measurement, the pump laser beam was chopped at 500 Hz. The delay between the pump and probe pulses was controlled by a motorized delay stage. The change in absorbance for the pumped and unpumped samples was calculated. Samples in 1 mm cuvettes were used for all spectroscopy measurements and stirred vigorously during the measurement to avoid the photocharging effects.[65] The solvent effect response is measured using the pure solvent solution. The excitation power of all the measurements is around 10 nJ/pulse, and the NR is confirmed under the single exciton region by performing a series of fluence-dependent studies (Figure S8).

Nanosecond TA. Nanosecond TA was performed with the EOS spectrometer (Ultrafast Systems LLC). The pump beam at 400 nm was generated in the same way as femtosecond TA experiments. The white light continuum (380−1700 nm, 0.5 ns pulse width, 20 kHz repetition rate) used here was generated by focusing an Nd:YAG laser into a photonic crystal fiber. The delay time between the pump and probe beam was controlled by a digital delay generator (CNT-90, Pendulum Instruments). The probe and reference beams were detected with the same multichannel spectrometers used in femtosecond TA experiments. The IRF of this system was measured to be ∼280 ps.

Temperature-Dependent FTIR. The 1-butanethiol (1-dodecanethiol) derivate-CdS NR is prepared by mixing 2 mL of CdS NRs (∼nmol, dissolved in 1:1 ratio chloroform/toluene mix solvent) with 100 μL of 1-butanethiol (1-dodecanethiol). The amount of 1-butanethiol (1-dodecanethiol) is set to be ∼10 times higher than that used in the MPA/MUA case in order to ensure the complete ligand exchange. The mixture is then vigorously stirred in the dark under ambient conditions overnight. After that, the CdS NR is precipitated with acetone. The samples are then redissolved in toluene and reprecipitated with ethanol for at least three times in order to remove all the residual ligands. The final sample is dried under vacuum and redissolved in 200 μL $CDCl_3$ (99.8%, Cambridge Isotope Laboratories, Inc.). The temperature-dependent Fourier transform infrared measurements were similar to previously described methods.[66] The infrared cell consisted of a copper housing that held two sandwiched CaF_2 windows vertically split by a 130 μm Teflon spacer. The sample and reference were injected into the separated halves of the cell with a gas-tight syringe. The cell was then placed on a copper block in a dry air-purged external sample compartment of a Varian 660 FTIR spectrometer. The block/cell position was controlled by a stepping motor drive (Mark-102, Sigma Koki). The temperature was controlled by a recirculating water bath

https://dx.doi.org/10.1021/acsami.0c07820
ACS Appl. Mater. Interfaces XXXX, XXX, XXX−XXX

and monitored with a thermocouple. Spectra of the sample and reference were collected at 1 cm^{-1} resolution between 10 and 55 °C in 5 °C increments, with the actual temperature at the sample read by a thermocouple. An equilibration time of at least 3 min was allowed for each temperature. The temperature-dependent FTIR data were processed by referencing the sample spectrum at a given temperature to the $CDCl_3$ reference measured at ∼10 °C ($A = -\log(I_{sample,T})/I_{reference,T}$).

■ ASSOCIATED CONTENT

Supporting Information

The Supporting Information is available free of charge at https://pubs.acs.org/doi/10.1021/acsami.0c07820.

Details of SFG measurements; calculation details; TEM and its statistical results; controlled H_2 production measurement of CdS/H_2ase without the redox mediator; complete sets of PDQ^{2+} reduction measurements for all the CdS NR samples capped with different mercapto-carboxylate ligands; complete sets of PDQ^{2+} titration measurements for all the CdS-NRs samples; TAS spectra fittings; and tables of the fitting parameters (PDF)

■ AUTHOR INFORMATION

Corresponding Authors

Wenxing Yang − *Department of Chemistry, Emory University, Atlanta, Georgia 30322, United States; Department of Chemistry—Ångström Laboratory, Physical Chemistry, Uppsala University, SE-75120 Uppsala, Sweden;* orcid.org/0000-0002-3440-9416; Email: wenxing.yang@emory.edu

R. Brian Dyer − *Department of Chemistry, Emory University, Atlanta, Georgia 30322, United States;* orcid.org/0000-0002-0090-7580; Email: briandyer@emory.edu

Tianquan Lian − *Department of Chemistry, Emory University, Atlanta, Georgia 30322, United States;* orcid.org/0000-0002-8351-3690; Email: tlian@emory.edu

Authors

Gregory E. Vansuch − *Department of Chemistry, Emory University, Atlanta, Georgia 30322, United States*

Yawei Liu − *Department of Chemistry, Emory University, Atlanta, Georgia 30322, United States*

Tao Jin − *Department of Chemistry, Emory University, Atlanta, Georgia 30322, United States*

Qiliang Liu − *Department of Chemistry, Emory University, Atlanta, Georgia 30322, United States*

Aimin Ge − *Department of Chemistry, Emory University, Atlanta, Georgia 30322, United States;* orcid.org/0000-0003-0127-3193

Monica L. K. Sanchez − *Department of Chemistry, Emory University, Atlanta, Georgia 30322, United States*

Dominik K. Haja − *Department of Biochemistry and Molecular Biology, University of Georgia, Athens, Georgia 30602, United States*

Michael W. W. Adams − *Department of Biochemistry and Molecular Biology, University of Georgia, Athens, Georgia 30602, United States*

Complete contact information is available at: https://pubs.acs.org/10.1021/acsami.0c07820

Notes

The authors declare no competing financial interest.

■ ACKNOWLEDGMENTS

This material is based upon work supported by the U.S. Department of Energy, Office of Science, Office of Basic Energy Sciences, Solar Photochemistry Program under Award DE-FG02-12ER16347 and DE-SC0008798 (to T.L.) and by the National Science Foundation under Award CHE1807865 and DMR 1808288 (to B.D). Some of the transient absorption measurements were conducted on a spectrometer supported by National Science Foundation MRI grant CHE-1726536. W.Y. acknowledges the financial support from the Swedish Research Council (Vetenskapsrådet) for an International Postdoc Fellowship (2017-00449). Dr. Alexey L. Kaledin, Dr. Bin Wang, and Dr. Laura M. Kiefer are acknowledged for their helpful discussions.

■ REFERENCES

(1) Garakyaraghi, S.; Castellano, F. N. Nanocrystals for Triplet Sensitization: Molecular Behavior from Quantum-Confined Materials. *Inorg. Chem.* **2018**, *57*, 2351−2359.

(2) Mongin, C.; Garakyaraghi, S.; Razgoniaeva, N.; Zamkov, M.; Castellano, F. N. Direct Observation of Triplet Energy Transfer from Semiconductor Nanocrystals. *Science* **2016**, *351*, 369−372.

(3) Huang, Z.; Li, X.; Mahboub, M.; Hanson, K. M.; Nichols, V. M.; Le, H.; Tang, M. L.; Bardeen, C. J. Hybrid Molecule-Nanocrystal Photon Upconversion Across the Visible and Near-Infrared. *Nano Lett.* **2015**, *15*, 5552−5557.

(4) Huang, Z.; Tang, M. L. Designing Transmitter Ligands That Mediate Energy Transfer between Semiconductor Nanocrystals and Molecules. *J. Am. Chem. Soc.* **2017**, *139*, 9412−9418.

(5) McClelland, K. P.; Weiss, E. A. Selective Photocatalytic Oxidation of Benzyl Alcohol to Benzaldehyde or C−C Coupled Products by Visible-Light-Absorbing Quantum Dots. *ACS Appl. Energy Mater.* **2019**, *2*, 92−96.

(6) Wang, K.; Lu, H.; Zhu, X.; Lin, Y.; Beard, M. C.; Yan, Y.; Chen, X. Ultrafast Reaction Mechanisms in Perovskite Based Photocatalytic C−C Coupling. *ACS Energy Lett.* **2020**, *5*, 566−571.

(7) Peterson, M. D.; Cass, L. C.; Harris, R. D.; Edme, K.; Sung, K.; Weiss, E. A. The Role of Ligands in Determining the Exciton Relaxation Dynamics in Semiconductor Quantum Dots. *Annu. Rev. Phys. Chem.* **2014**, *65*, 317−339.

(8) Brown, P. R.; Kim, D.; Lunt, R. R.; Zhao, N.; Bawendi, M. G.; Grossman, J. C.; Bulović, V. Energy Level Modification in Lead Sulfide Quantum Dot Thin Films through Ligand Exchange. *ACS Nano* **2014**, *8*, 5863−5872.

(9) Kroupa, D. M.; Vörös, M.; Brawand, N. P.; McNichols, B. W.; Miller, E. M.; Gu, J.; Nozik, A. J.; Sellinger, A.; Galli, G.; Beard, M. C. Tuning Colloidal Quantum Dot Band Edge Positions through Solution-Phase Surface Chemistry Modification. *Nat. Commun.* **2017**, *8*, 15257.

(10) Wang, H. I.; Lu, H.; Nagata, Y.; Bonn, M.; Cánovas, E. Dipolar Molecular Capping in Quantum Dot-Sensitized Oxides: Fermi Level Pinning Precludes Tuning Donor-Acceptor Energetics. *ACS Nano* **2017**, *11*, 4760−4767.

(11) Tagliazucchi, M.; Tice, D. B.; Sweeney, C. M.; Morris-Cohen, A. J.; Weiss, E. A. Ligand-Controlled Rates of Photoinduced Electron Transfer in Hybrid CdSe Nanocrystal/Poly(Viologen) Films. *ACS Nano* **2011**, *5*, 9907−9917.

(12) Wilker, M. B.; Utterback, J. K.; Greene, S.; Brown, K. A.; Mulder, D. W.; King, P. W.; Dukovic, G. Role of Surface-Capping Ligands in Photoexcited Electron Transfer between CdS Nanorods and [FeFe] Hydrogenase and the Subsequent H_2 Generation. *J. Phys. Chem. C* **2018**, *122*, 741−750.

(13) Boles, M. A.; Engel, M.; Talapin, D. V. Self-Assembly of Colloidal Nanocrystals: From Intricate Structures to Functional Materials. *Chem. Rev.* **2016**, *116*, 11220−11289.

(14) Delehanty, J. B.; Medintz, I. L.; Pons, T.; Brunel, F. M.; Dawson, P. E.; Mattoussi, H. Self-Assembled Quantum Dot−Peptide

Bioconjugates for Selective Intracellular Delivery. *Bioconjugate Chem.* **2006**, *17*, 920−927.
(15) Brown, K. A.; Harris, D. F.; Wilker, M. B.; Rasmussen, A.; Khadka, N.; Hamby, H.; Keable, S.; Dukovic, G.; Peters, J. W.; Seefeldt, L. C.; King, P. W. Light-Driven Dinitrogen Reduction Catalyzed by a CdS:Nitrogenase MoFe Protein Biohybrid. *Science* **2016**, *352*, 448−450.
(16) Chica, B.; Wu, C.-H.; Liu, Y.; Adams, M. W. W.; Lian, T.; Dyer, R. B. Balancing Electron Transfer Rate and Driving Force for Efficient Photocatalytic Hydrogen Production in CdSe/CdS Nanorod−[NiFe] Hydrogenase Assemblies. *Energy Environ. Sci.* **2017**, *10*, 2245−2255.
(17) Wilker, M. B.; Shinopoulos, K. E.; Brown, K. A.; Mulder, D. W.; King, P. W.; Dukovic, G. Electron Transfer Kinetics in CdS Nanorod−[FeFe]-Hydrogenase Complexes and Implications for Photochemical H 2 Generation. *J. Am. Chem. Soc.* **2014**, *136*, 4316−4324.
(18) Brown, K. A.; Dayal, S.; Ai, X.; Rumbles, G.; King, P. W. Controlled Assembly of Hydrogenase-CdTe Nanocrystal Hybrids for Solar Hydrogen Production. *J. Am. Chem. Soc.* **2010**, *132*, 9672−9680.
(19) Brown, K. A.; Song, Q.; Mulder, D. W.; King, P. W. Diameter Dependent Electron Transfer Kinetics in Semiconductor−Enzyme Complexes. *ACS Nano* **2014**, *8*, 10790−10798.
(20) Bruno, L. Summary for Policymakers. In *Climate Change 2013—The Physical Science Basis; Intergovernmental Panel on Climate Change*; Cambridge University Press: Cambridge, 2019; Vol. *53*, pp 1−30.
(21) Utterback, J. K.; Wilker, M. B.; Mulder, D. W.; King, P. W.; Eaves, J. D.; Dukovic, G. Quantum Efficiency of Charge Transfer Competing against Nonexponential Processes: The Case of Electron Transfer from CdS Nanorods to Hydrogenase. *J. Phys. Chem. C* **2019**, *123*, 886−896.
(22) Sanchez, M. L. K.; Wu, C.-H.; Adams, M. W. W.; Dyer, R. B. Optimizing Electron Transfer from CdSe QDs to Hydrogenase for Photocatalytic H_2 Production. *Chem. Commun.* **2019**, *55*, 5579−5582.
(23) Cohn, A. W.; Janßen, N.; Mayer, J. M.; Gamelin, D. R. Photocharging ZnO Nanocrystals: Picosecond Hole Capture, Electron Accumulation, and Auger Recombination. *J. Phys. Chem. C* **2012**, *116*, 20633−20642.
(24) Reisner, E. Solar Hydrogen Evolution with Hydrogenases: From Natural to Hybrid Systems. *Eur. J. Inorg. Chem.* **2011**, *2011*, 1005−1016.
(25) Morris-Cohen, A. J.; Peterson, M. D.; Frederick, M. T.; Kamm, J. M.; Weiss, E. A. Evidence for a Through-Space Pathway for Electron Transfer from Quantum Dots to Carboxylate-Functionalized Viologens. *J. Phys. Chem. Lett.* **2012**, *3*, 2840−2844.
(26) Morris-Cohen, A. J.; Vasilenko, V.; Amin, V. A.; Reuter, M. G.; Weiss, E. A. Model for Adsorption of Ligands to Colloidal Quantum Dots with Concentration-Dependent Surface Structure. *ACS Nano* **2012**, *6*, 557−565.
(27) Sokol, K. P.; Robinson, W. E.; Warnan, J.; Kornienko, N.; Nowaczyk, M. M.; Ruff, A.; Zhang, J. Z.; Reisner, E. Bias-Free Photoelectrochemical Water Splitting with Photosystem II on a Dye-Sensitized Photoanode Wired to Hydrogenase. *Nat. Energy* **2018**, *3*, 944−951.
(28) Kornienko, N.; Zhang, J. Z.; Sakimoto, K. K.; Yang, P.; Reisner, E. Interfacing Nature's Catalytic Machinery with Synthetic Materials for Semi-Artificial Photosynthesis. *Nat. Nanotechnol.* **2018**, *13*, 890−899.
(29) Wu, C.-H.; McTernan, P. M.; Walter, M. E.; Adams, M. W. W. Production and Application of a Soluble Hydrogenase from Pyrococcus Furiosus. *Archaea* **2015**, *2015*, 1−8.
(30) Ben-Shahar, Y.; Scotognella, F.; Waiskopf, N.; Kriegel, I.; Dal Conte, S.; Cerullo, G.; Banin, U. Effect of Surface Coating on the Photocatalytic Function of Hybrid CdS-Au Nanorods. *Small* **2015**, *11*, 462−471.
(31) Wu, K.; Rodríguez-Córdoba, W.; Lian, T. Exciton Localization and Dissociation Dynamics in CdS and CdS−Pt Quantum Confined Nanorods: Effect of Nonuniform Rod Diameters. *J. Phys. Chem. B* **2014**, *118*, 14062−14069.
(32) Borys, N. J.; Walter, M. J.; Huang, J.; Talapin, D. V.; Lupton, J. M. The Role of Particle Morphology in Interfacial Energy Transfer in CdSe/CdS Heterostructure Nanocrystals. *Science* **2010**, *330*, 1371−1374.
(33) Schapotschnikow, P.; Hommersom, B.; Vlugt, T. J. H. Adsorption and Binding of Ligands to CdSe Nanocrystals. *J. Phys. Chem. C* **2009**, *113*, 12690−12698.
(34) Wu, K.; Zhu, H.; Liu, Z.; Rodríguez-Córdoba, W.; Lian, T. Ultrafast Charge Separation and Long-Lived Charge Separated State in Photocatalytic CdS−Pt Nanorod Heterostructures. *J. Am. Chem. Soc.* **2012**, *134*, 10337−10340.
(35) Wu, K.; Chen, Z.; Lv, H.; Zhu, H.; Hill, C. L.; Lian, T. Hole Removal Rate Limits Photodriven H 2 Generation Efficiency in CdS-Pt and CdSe/CdS-Pt Semiconductor Nanorod−Metal Tip Heterostructures. *J. Am. Chem. Soc.* **2014**, *136*, 7708−7716.
(36) Geva, N.; Shepherd, J. J.; Nienhaus, L.; Bawendi, M. G.; Van Voorhis, T. Morphology of Passivating Organic Ligands around a Nanocrystal. *J. Phys. Chem. C* **2018**, *122*, 26267−26274.
(37) Utterback, J. K.; Grennell, A. N.; Wilker, M. B.; Pearce, O. M.; Eaves, J. D.; Dukovic, G. Observation of Trapped-Hole Diffusion on the Surfaces of CdS Nanorods. *Nat. Chem.* **2016**, *8*, 1061−1066.
(38) Wu, K.; Du, Y.; Tang, H.; Chen, Z.; Lian, T. Efficient Extraction of Trapped Holes from Colloidal CdS Nanorods. *J. Am. Chem. Soc.* **2015**, *137*, 10224−10230.
(39) Zhu, H.; Song, N.; Lv, H.; Hill, C. L.; Lian, T. Near Unity Quantum Yield of Light-Driven Redox Mediator Reduction and Efficient H 2 Generation Using Colloidal Nanorod Heterostructures. *J. Am. Chem. Soc.* **2012**, *134*, 11701−11708.
(40) Zhao, F.; Li, Q.; Han, K.; Lian, T. Mechanism of Efficient Viologen Radical Generation by Ultrafast Electron Transfer from CdS Quantum Dots. *J. Phys. Chem. C* **2018**, *122*, 17136−17142.
(41) Morris-Cohen, A. J.; Frederick, M. T.; Cass, L. C.; Weiss, E. A. Simultaneous Determination of the Adsorption Constant and the Photoinduced Electron Transfer Rate for a Cds Quantum Dot−Viologen Complex. *J. Am. Chem. Soc.* **2011**, *133*, 10146−10154.
(42) Chen, J.; Wu, K.; Rudshteyn, B.; Jia, Y.; Ding, W.; Xie, Z.-X.; Batista, V. S.; Lian, T. Ultrafast Photoinduced Interfacial Proton Coupled Electron Transfer from CdSe Quantum Dots to 4,4′-Bipyridine. *J. Am. Chem. Soc.* **2016**, *138*, 884−892.
(43) Tachiya, M. Kinetics of Quenching of Luminescent Probes in Micellar Systems. II. *J. Chem. Phys.* **1982**, *76*, 340−348.
(44) Tachiya, M. Application of a Generating Function to Reaction Kinetics in Micelles. Kinetics of Quenching of Luminescent Probes in Micelles. *Chem. Phys. Lett.* **1975**, *33*, 289−292.
(45) Huang, J.; Huang, Z.; Yang, Y.; Zhu, H.; Lian, T. Multiple Exciton Dissociation in CdSe Quantum Dots by Ultrafast Electron Transfer to Adsorbed Methylene Blue. *J. Am. Chem. Soc.* **2010**, *132*, 4858−4864.
(46) Morris-Cohen, A. J.; Peterson, M. D.; Frederick, M. T.; Kamm, J. M.; Weiss, E. A. Evidence for a Through-Space Pathway for Electron Transfer from Quantum Dots to Carboxylate-Functionalized Viologens. *J. Phys. Chem. Lett.* **2012**, *3*, 2840−2844.
(47) Chen, J.; Wu, K.; Rudshteyn, B.; Jia, Y.; Ding, W.; Xie, Z.-X.; Batista, V. S.; Lian, T. Ultrafast Photoinduced Interfacial Proton Coupled Electron Transfer from CdSe Quantum Dots to 4,4′-Bipyridine. *J. Am. Chem. Soc.* **2016**, *138*, 884−892.
(48) Porter, M. D.; Bright, T. B.; Allara, D. L.; Chidsey, C. E. D. Spontaneously Organized Molecular Assemblies. 4. Structural Characterization of n-Alkyl Thiol Monolayers on Gold by Optical Ellipsometry, Infrared Spectroscopy, and Electrochemistry. *J. Am. Chem. Soc.* **1987**, *109*, 3559−3568.
(49) Badia, A.; Cuccia, L.; Demers, L.; Morin, F.; Lennox, R. B. Structure and Dynamics in Alkanethiolate Monolayers Self-Assembled on Gold Nanoparticles: A DSC, FT-IR, and Deuterium NMR Study. *J. Am. Chem. Soc.* **1997**, *119*, 2682−2692.
(50) Fies, W. A.; Dugger, J. W.; Dick, J. E.; Wilder, L. M.; Browning, K. L.; Doucet, M.; Browning, J. F.; Webb, L. J. Direct Measurement of Water Permeation in Submerged Alkyl Thiol Self-Assembled

https://dx.doi.org/10.1021/acsami.0c07820
ACS Appl. Mater. Interfaces XXXX, XXX, XXX−XXX

Monolayers on Gold Surfaces Revealed by Neutron Reflectometry. *Langmuir* **2019**, *35*, 5647−5662.
(51) Nuzzo, R. G.; Dubois, L. H.; Allara, D. L. Fundamental Studies of Microscopic Wetting on Organic Surfaces. 1. Formation and Structural Characterization of a Self-Consistent Series of Polyfunctional Organic Monolayers. *J. Am. Chem. Soc.* **1990**, *112*, 558−569.
(52) Chen, J.; Wang, Z.; Oyola-Reynoso, S.; Thuo, M. M. Properties of Self-Assembled Monolayers Revealed via Inverse Tensiometry. *Langmuir* **2017**, *33*, 13451−13467.
(53) Chen, J.; Chang, B.; Oyola-Reynoso, S.; Wang, Z.; Thuo, M. Quantifying Gauche Defects and Phase Evolution in Self-Assembled Monolayers through Sessile Drops. *ACS Omega* **2017**, *2*, 2072−2084.
(54) Ge, A.; Rudshteyn, B.; Videla, P. E.; Miller, C. J.; Kubiak, C. P.; Batista, V. S.; Lian, T. Heterogenized Molecular Catalysts: Vibrational Sum-Frequency Spectroscopic, Electrochemical, and Theoretical Investigations. *Acc. Chem. Res.* **2019**, *52*, 1289.
(55) Clark, M. L.; Ge, A.; Videla, P. E.; Rudshteyn, B.; Miller, C. J.; Song, J.; Batista, V. S.; Lian, T.; Kubiak, C. P. CO 2 Reduction Catalysts on Gold Electrode Surfaces Influenced by Large Electric Fields. *J. Am. Chem. Soc.* **2018**, *140*, 17643−17655.
(56) Ge, A.; Videla, P. E.; Lee, G. L.; Rudshteyn, B.; Song, J.; Kubiak, C. P.; Batista, V. S.; Lian, T. Interfacial Structure and Electric Field Probed by in Situ Electrochemical Vibrational Stark Effect Spectroscopy and Computational Modeling. *J. Phys. Chem. C* **2017**, *121*, 18674−18682.
(57) Himmelhaus, M.; Eisert, F.; Buck, M.; Grunze, M. Self-Assembly of n-Alkanethiol Monolayers. a Study by IR-Visible Sum Frequency Spectroscopy (SFG). *J. Phys. Chem. B* **2000**, *104*, 576−584.
(58) Zhuang, X.; Miranda, P. B.; Kim, D.; Shen, Y. R. Mapping Molecular Orientation and Conformation at Interfaces by Surface Nonlinear Optics. *Phys. Rev. B: Condens. Matter Mater. Phys.* **1999**, *59*, 12632−12640.
(59) Weeraman, C.; Yatawara, A. K.; Bordenyuk, A. N.; Benderskii, A. V. Effect of Nanoscale Geometry on Molecular Conformation: Vibrational Sum-Frequency Generation of Alkanethiols on Gold Nanoparticles. *J. Am. Chem. Soc.* **2006**, *128*, 14244−14245.
(60) Murphy, M. W.; Yiu, Y. M.; Ward, M. J.; Liu, L.; Hu, Y.; Zapien, J. A.; Liu, Y.; Sham, T. K. Electronic Structure and Optical Properties of CdSxSe1−x Solid Solution Nanostructures from X-Ray Absorption near Edge Structure, X-Ray Excited Optical Luminescence, and Density Functional Theory Investigations. *J. Appl. Phys.* **2014**, *116*, 193709.
(61) Balan, A. D.; Olshansky, J. H.; Horowitz, Y.; Han, H.-L.; O'Brien, E. A.; Tang, L.; Somorjai, G. A.; Alivisatos, A. P. Unsaturated Ligands Seed an Order to Disorder Transition in Mixed Ligand Shells of CdSe/CdS Quantum Dots. *ACS Nano* **2019**, *13*, 13784.
(62) Hildebrandt, N.; Spillmann, C. M.; Algar, W. R.; Pons, T.; Stewart, M. H.; Oh, E.; Susumu, K.; Díaz, S. A.; Delehanty, J. B.; Medintz, I. L. Energy Transfer with Semiconductor Quantum Dot Bioconjugates: A Versatile Platform for Biosensing, Energy Harvesting, and Other Developing Applications. *Chem. Rev.* **2017**, *117*, 536−711.
(63) Melle, S.; Calderón, O. G.; Laurenti, M.; Mendez-Gonzalez, D.; Egatz-Gómez, A.; López-Cabarcos, E.; Cabrera-Granado, E.; Díaz, E.; Rubio-Retama, J. Förster Resonance Energy Transfer Distance Dependence from Upconverting Nanoparticles to Quantum Dots. *J. Phys. Chem. C* **2018**, *122*, 18751−18758.
(64) Acharya, K. P.; Khnayzer, R. S.; O'Connor, T.; Diederich, G.; Kirsanova, M.; Klinkova, A.; Roth, D.; Kinder, E.; Imboden, M.; Zamkov, M.; et al. The Role of Hole Localization in Sacrificial Hydrogen Production by Semiconductor−Metal Heterostructured Nanocrystals. *Nano Lett.* **2011**, *11*, 2919−2926.
(65) McGuire, J. A.; Sykora, M.; Robel, I.; Padilha, L. A.; Joo, J.; Pietryga, J. M.; Klimov, V. I. Spectroscopic Signatures of Photocharging Due to Hot-Carrier Transfer in Solutions of Semiconductor Nanocrystals under Low-Intensity Ultraviolet Excitation. *ACS Nano* **2010**, *4*, 6087−6097.
(66) Zhao, J.; Su, H.; Vansuch, G. E.; Liu, Z.; Salaita, K.; Dyer, R. B. Localized Nanoscale Heating Leads to Ultrafast Hydrogel Volume-Phase Transition. *ACS Nano* **2019**, *13*, 515−525.

https://dx.doi.org/10.1021/acsami.0c07820
ACS Appl. Mater. Interfaces XXXX, XXX, XXX−XXX